Environmental Science and Ecotechnology 31 (2026) 100696

Contents lists available at ScienceDirect

Environmental Science and Ecotechnology

journal homepage: www.journals.elsevier.com/environmental-science-and-ecotechnology/

Original Research

Phase-change photothermal foam enables continuous hypersaline brine desalination

Peilei Zhou [a], Feng Sun [b], Lishan Xu [a], Qingshan Liu [c], Jia Xu [a,*]

[a] Key Laboratory of Marine Chemistry Theory and Technology, Ministry of Education, College of Chemistry and Chemical Engineering, Ocean University of China, Qingdao, Shandong, 266100, China
[b] School of Materials Science and Engineering, Ocean University of China, Qingdao, Shandong, 266100, China
[c] School of Life Sciences, Huzhou University, Huzhou, Zhejiang, 313000, China

ARTICLE INFO

Article history:
Received 31 August 2025
Received in revised form
31 March 2026
Accepted 2 April 2026

Keywords:
Solar-driven seawater desalination
Phase change material
Water treatment

ABSTRACT

Seawater desalination is critical for mitigating global freshwater scarcity, yet the discharge of high-salinity brine causes severe ecological and economic issues. Solar-driven interfacial evaporation provides an energy-efficient method for achieving zero liquid discharge and effective brine concentration. To manage the inherent intermittency of natural sunlight, phase change materials are increasingly integrated to store excess thermal energy for continuous evaporation. Nevertheless, current systems are limited by elevated phase-transition temperatures, liquid leakage, and substantial performance degradation in hypersaline conditions. Here we show a multifunctional composite foam that unifies broadband photothermal conversion with low-temperature phase-change thermal regulation for sustained hypersaline desalination. By confining dodecylamine within a polypyrrole-coated chitosan-phenolic network, our material achieves a 95% solar absorption efficiency and a phase-change energy storage capacity of 208.4 J g^{-1}. The evaporator achieves a stable evaporation rate of 1.862 kg m^{-2} h^{-1} under one sun and maintains 0.684 kg m^{-2} h^{-1} in the absence of light. It also sustains a high evaporation rate of 1.763 kg m^{-2} h^{-1} in 20 wt% NaCl without salt accumulation and produces 9.229 kg m^{-2} of purified freshwater over 10 h of outdoor solar operation. These findings provide a scalable and continuous approach to solar-driven brine reduction, advancing sustainable resource recovery and all-weather water purification.

1. Introduction

Seawater desalination has emerged as an effective approach to mitigating global freshwater scarcity, and its scale and number of installations have steadily increased in recent years [1–3]. However, this process unavoidably generates large volumes of concentrated brine, particularly under high-recovery operating conditions [4–6]. Such brine not only contains high levels of dissolved salts (e.g., NaCl, $CaSO_4$, $MgCl_2$) [7] but may also accumulate residual pretreatment chemicals, heavy metals, and organic contaminants [8–10]. The untreated discharge of brine presents serious threats to marine ecosystems, including elevated salinity, thermal pollution, and eutrophication [9,11]. In inland regions, deep-well injection is both costly and associated with the risk of groundwater contamination. Therefore, the minimization, safe disposal, and resource recovery of brine represent pressing challenges for the sustainable development of seawater desalination [12–15]. At present, the primary treatment pathways for hypersaline wastewater include thermal processes (e.g., multistage flash distillation [16]; multieffect distillation [17]; mechanical vapor compression [18]) and membrane processes (e.g., reverse osmosis [19]; membrane distillation [20]). However, these methods are hindered by high energy demand, severe scaling, and prohibitive operating costs. Under the strategic framework of zero liquid discharge, developing green, energy-efficient, and economically viable technologies for brine concentration and resource recovery has become an urgent priority [15,21–23].

Solar-driven interfacial evaporation (SDIE) enables efficient energy concentration at the water–air interface, thereby achieving highly effective evaporation while suppressing salt crystallization

* Corresponding author.
E-mail address: qdxujia@sina.com.cn (J. Xu).

https://doi.org/10.1016/j.ese.2026.100696

[24–27]. Even in high-salinity brine environments, it can continuously evaporate to produce freshwater while further concentrating the brine. By utilizing renewable energy with a low carbon footprint and tunable thermal management capabilities, SDIE offers a promising pathway to reduce high-salinity brine and recover salt resources [28–30]. In recent years, SDIE systems have achieved remarkable advances through the rational design of photothermal conversion materials that exhibit strong light absorption, high localized thermal capacity, and superior salt resistance, alongside the construction of efficient water-transport architectures and the optimization of interfacial heat transfer [31–33]. These developments have substantially improved photothermal conversion efficiency, evaporation rates, and long-term operational stability [34–36]. Specifically, under 1 sun of solar irradiation, the evaporation rate has increased from approximately 0.3–0.5 kg m^{-2} h^{-1} for pure water to 1.0–1.5 kg m^{-2} h^{-1} for typical interfacial evaporators, while some advanced systems can even reach about 2.0 kg m^{-2} h^{-1}. At the same time, the solar absorption efficiency of optimized photothermal materials typically exceeds 90%. Nonetheless, the practical implementation of this technology remains constrained by the inherent variability of natural solar irradiance. Periodic fluctuations in sunlight and climatic variability can induce discontinuities in the interfacial evaporation process, thereby limiting freshwater yield and the efficiency of brine concentration [37,38]. To address these issues, phase change materials (PCMs) are introduced into the SDIE system to store and release excess photothermal energy while maintaining continuous evaporation under unstable light conditions. However, existing PCMs (such as polyethylene glycol (PEG) and paraffin systems) still face several significant problems in practical applications, limiting their widespread use. First, these traditional PCMs have relatively high phase-transition temperatures, with PEG and paraffin undergoing phase transitions at 62.45 and 46.5 °C, respectively. These high phase-transition temperatures prevent them from reaching the material's phase-transition conditions under low irradiation and environmental fluctuations, making it difficult to store and release heat quickly and efficiently. As a result, the stability and efficiency of the evaporation process are significantly reduced, with the PI/MXene/PEG and O-VG-CC exhibiting evaporation rates of 1.24 and 1.36 kg m^{-2} h^{-1}, respectively. Second, existing PCMs often suffer from leakage of liquid-phase material during phase transitions, leading to material failure and affecting the system's long-term stability. Furthermore, traditional phase change materials tend to experience performance degradation after multiple heating–cooling cycles, severely affecting their cyclic stability and sustainability [39,40].

This study presents a sustainable photothermal composite foam, PPy-CS/PF@DDA (PF: phenolic resin), designed to address the limitations of traditional phase change materials, particularly their relatively high phase-transition temperatures and insufficient structural stability. By introducing dodecylamine (DDA) as the phase change component, the composite is able to respond more readily to mild thermal input and low-light conditions, which is beneficial for improving heat utilization and sustaining water evaporation under fluctuating solar irradiation. Chitosan (CS), with its intrinsic hydrophilicity and abundant functional groups, facilitates water transport, while its chemical crosslinking with phenolic resin enhances the mechanical robustness and structural integrity of the foam. The porous CS/PF framework also helps confine the phase change component, contributing to the thermal stability of the composite during repeated phase transitions. In addition, the *in situ* polymerized polypyrrole (PPy) layer endows the material with efficient broadband solar absorption, promoting localized heating and improved photothermal conversion. As a result, the integrated material exhibits promising solar-driven evaporation performance, good salt resistance, favorable cycling stability, and effective water purification capability. By combining a biomass-derived hydrophilic scaffold, phase-change thermal regulation, and broadband photothermal conversion within a single system, this work provides a feasible strategy for developing durable and scalable evaporators for high-salinity desalination and wastewater treatment applications.

2. Materials and methods

2.1. Materials

Formaldehyde solution (37%) and chitosan were purchased from Tokyo Chemical Industry Co., Ltd., China. Phenol was obtained from Sinopharm Chemical Reagent Co., Ltd. Phytic acid solution (50 wt%), dodecylamine, and pyrrole (99%) were provided by Shanghai Macklin Biochemical Co., Ltd. The pyrrole was further purified using a rotary evaporator. Moreover, the details of the Characterization are provided in Supplementary Text S1.

2.2. Synthesis of CS/PF foam

The CS/PF foam was prepared via a typical sol–gel method. Initially, 0.4 g of CS was dissolved in a mixed solution containing 1.5 mL of hydrochloric acid and 15 mL of absolute ethanol. The mixture was stirred at room temperature until a uniform, transparent sol was formed. Subsequently, 1.6 g of phenol and 5 mL of 37 wt% formaldehyde solution were sequentially added to the sol, and stirring was continued until all components had dissolved to give a clear gel precursor. The resulting precursor was then transferred to a sealed autoclave and heated at 120 °C for 12 h to facilitate gelation and aging during the sol–gel transition. After the reaction, an orange–yellow porous gel was obtained. The gel was thoroughly washed and soaked in deionized water 2–3 times to remove unreacted reagents and by-products. A structurally stable CS/PF composite foam was finally obtained.

2.3. Polypyrrole modification of PPy-CS/PF foam

The polypyrrole-coated CS/PF foam (PPy-CS/PF) was prepared via a solid–liquid interfacial polymerization method. Briefly, 13.7 g of ammonium persulfate was dissolved in 25 mL of deionized water and cooled to 0 °C in an ice bath to obtain the oxidant solution (solution A). Simultaneously, 4.2 mL of pyrrole monomer, 25 mL of isopropanol, and 9.2 mL of 50 wt% phytic acid solution were mixed thoroughly and cooled to 0 °C to form the monomer solution (solution B). During polymerization, solutions A and B were sequentially sprayed onto the surface of the preformed CS/PF foam, with a final layer of solution A completing one deposition cycle [41]. This three-step spraying process was repeated three times to ensure uniform and sufficient deposition of PPy onto the foam skeleton. The gradual color change of the foam from orange to black indicated the successful formation of the PPy layer. Finally, the composite was thoroughly rinsed with deionized water 2–3 times to remove unreacted monomers and by-products, yielding the structurally stable PPy-CS/PF composite foam.

2.4. Synthesis and preparation of PPy-CS/PF@DDA

Dodecylamine was preheated to 40 °C in a vacuum oven until completely liquefied. The PPy-CS/PF foam was then immersed in the molten DDA under vacuum to promote deep infiltration into the porous network. Owing to the strong capillary action of the aerogel-like structure, the molten DDA was spontaneously drawn into the internal pores of the foam. After sufficient impregnation,

the composite was removed and placed on weighing paper to remove any excess DDA adhering to the surface. This step was repeated until no visible residue of DDA remained on the paper and the composite's total mass stabilized. DDA impregnation was then considered complete.

3. Results and discussion

3.1. Characterization of the structure and morphology of the sample

The PPy-CS/PF@DDA foam was synthesized via a combination of sol–gel processing and vacuum-assisted impregnation of a phase change material (Fig. 1). Initially, CS was dissolved in an acidic ethanol solution containing hydrochloric acid to form a homogeneous solution. Subsequently, phenol and formaldehyde were sequentially introduced into the system under continuous stirring at room temperature to ensure complete dissolution of all components. The resulting transparent sol was then subjected to thermal treatment at 120 °C for 12 h to induce the sol–gel transition. During this stage, formaldehyde participated in both the polycondensation of phenol and the cross-linking of chitosan, resulting in a durable three-dimensional porous CS/PF foam network. To improve the photothermal conversion capability of the foam, PPy was deposited on the surface of the preformed CS/PF structure via an *in situ* solid–liquid interfacial polymerization process. This coating endowed the foam with improved solar absorption and thermal responsiveness. Following polymerization, DDA, a phase-change material, was introduced into the porous matrix. The DDA was first heated to 40 °C to melt, then absorbed into the foam structure under vacuum via capillary forces, thereby forming the composite PPy-CS/PF@DDA.

To gain further insight into the morphological evolution of the composite foam, scanning electron microscopy images at various stages of synthesis (Fig. 1b–d). The three-dimensional cross-linked structure of the original CS/PF foam (Fig. 1b), which exhibits good continuity and grape-like morphology [42]. This structure reflects the successful formation of a stable porous framework via the sol–gel process. After the *in situ* polymerization of PPy, the surface morphology of the foam changes noticeably (Fig. 1c). Although the underlying three-dimensional network remains intact, the surface becomes significantly rougher, consistent with the formation of a PPy coating. This observation is further supported by X-ray photoelectron spectroscopy (XPS) analysis, which reveals the presence of nitrogen-an element characteristic of PPy on the foam surface, thereby confirming successful deposition. The internal structure of the final composite (Fig. 1d) clearly shows that the interconnected pores of the foam are filled with DDA. This demonstrates the efficient infiltration and uniform distribution of the phase change material within the porous matrix, attributed to capillary-driven absorption under vacuum conditions [43]. The PPy-CS/PF foam has a diameter of approximately 2.1 cm and an apparent density of 0.187 g cm^{-3} (Fig. 1e). Due to its ultralight nature, the foam can be placed on delicate surfaces, such as flower petals, without causing deformation (Fig. 1f). Furthermore, the foam exhibits excellent mechanical robustness, as it can withstand a 500 g load without noticeable deformation or structural collapse (Fig. 1g).

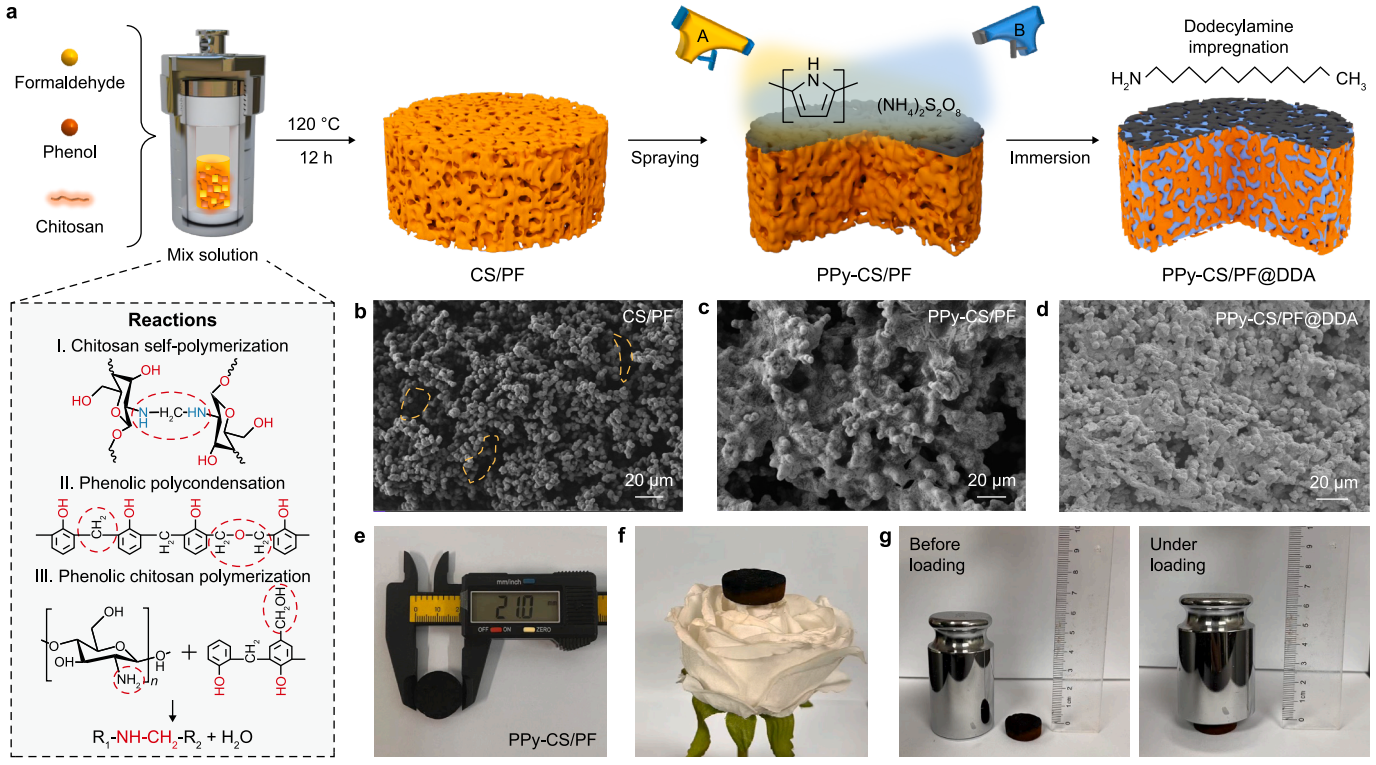

Fig. 1. Fabrication process and structural features of the PPy-CS/PF@DDA evaporator. a, Schematic illustration of the preparation route of PPy-CS/PF@DDA, including the deposition of polypyrrole (PPy) on the chitosan/phenolic resin (CS/PF) framework using oxidant solution A and monomer solution B, followed by dodecylamine (DDA) impregnation. Red dashed circles indicate the specific reaction sites among the different monomer components. **b–d**, Scanning electron microscopy images of CS/PF (**b**), PPy-CS/PF (**c**), and PPy-CS/PF@DDA (**d**). The yellow dashed outlines highlight representative formed pore-structure regions. **e**, Digital photograph of PPy-CS/PF@DDA. **f**, Digital photograph of PPy-CS/PF@DDA placed on a flower, demonstrating its ultralight nature. **g**, Digital photographs showing that PPy-CS/PF@DDA can withstand a weight of 500 g, indicating its good mechanical properties.

We employed Fourier transform infrared spectroscopy (FTIR) and XPS (Supplementary Fig. S1) to further validate the chemical reaction mechanisms and hybrid cross-linking behavior among the components. In the FTIR spectrum (Fig. 2c), chitosan showed characteristic absorption peaks at 1633 and 1602 cm^{-1}, corresponding to the stretching vibration of primary amines (C–N) and the bending vibration of amino groups (–NH), respectively [44,45]. These peaks represent the inherent functional groups of chitosan prior to chemical cross-linking. Compared with pure PF foam, the intensity of these characteristic peaks is significantly attenuated in the CS/PF composite, indicating that the amino groups in chitosan have undergone chemical cross-linking with the aldehyde groups formed during the ring-opening of phenol-formaldehyde resin. This reaction, a classical amino-aldehyde condensation (also known as the Maillard reaction) [46], forms stable covalent bonds and facilitates the formation of a three-dimensional, cross-linked hybrid network. Further insight into the bonding environment was obtained from the high-resolution XPS spectra of C 1s and N 1s. The C 1s spectrum exhibits peaks at 285.5 and 286.5 eV, corresponding to C–N and C–O bonds, respectively [47]. These features suggest that the amino groups of chitosan react with the hydroxymethyl groups of PF, forming amide-like linkages, while the continued self-condensation of PF forms methylene or methylene ether bridges. Furthermore, the N 1s spectrum shows a peak at approximately 400.0 eV, assigned to N–C bonding, further confirming the successful chemical integration of chitosan into the PF network (Fig. 2b) [48,49]. Collectively, these FTIR and XPS results confirm that chitosan is successfully incorporated into the CS/PF foam and actively participates in covalent cross-linking, resulting in a structurally stable three-dimensional hybrid network.

The thermal stability of CS/PF and PPy-CS/PF@DDA composites was systematically investigated via thermogravimetric analysis (Fig. 2d). For the CS/PF sample, a minor weight loss was observed in the temperature range from room temperature to 100 °C, which can be ascribed to the evaporation of physically adsorbed moisture. As the temperature increased to approximately 400 °C, a more pronounced mass loss occurred, primarily due to the thermal degradation of low-molecular-weight components. Upon further heating to 600 °C, the residual mass of CS/PF stabilized at approximately 30%, indicating moderate thermal stability. In comparison, the PPy-CS/PF@DDA composite exhibited a higher rate of thermal degradation, mainly attributed to the lower initial decomposition temperature of DDA and its relatively high content within the composite [50]. However, the porous structure of the CS/PF matrix played an important role in retarding the diffusion and volatilization of DDA, thereby reducing the overall mass-loss rate. At 600 °C, the residual mass of PPy-CS/PF@DDA was approximately 10%, indicating that the composite retains some thermal stability even at elevated temperatures.

We investigated the thermal energy storage capacity and phase-change behavior of pure DDA and the PPy-CS/PF@DDA composite by differential scanning calorimetry (DSC) (Fig. 2e and f). The DSC thermograms reveal that both pure DDA and PPy-CS/PF@DDA exhibit distinct endothermic melting peaks and exothermic crystallization peaks with similar peak profiles. This indicates that the phase-change behavior of the composite is primarily governed by the incorporated DDA, which retains its intrinsic phase-transition properties within the composite matrix. Specifically, during cooling, pure DDA exhibits a well-defined crystallization peak at 24.03 °C. Upon heating, the melting point is 29.8 °C. The corresponding crystallization and melting enthalpies are 280.7 and 279.3 J g^{-1}, respectively, demonstrating the high latent heat storage capacity of DDA (Supplementary Table S1). For the PPy-CS/PF@DDA foam, although the crystallization and

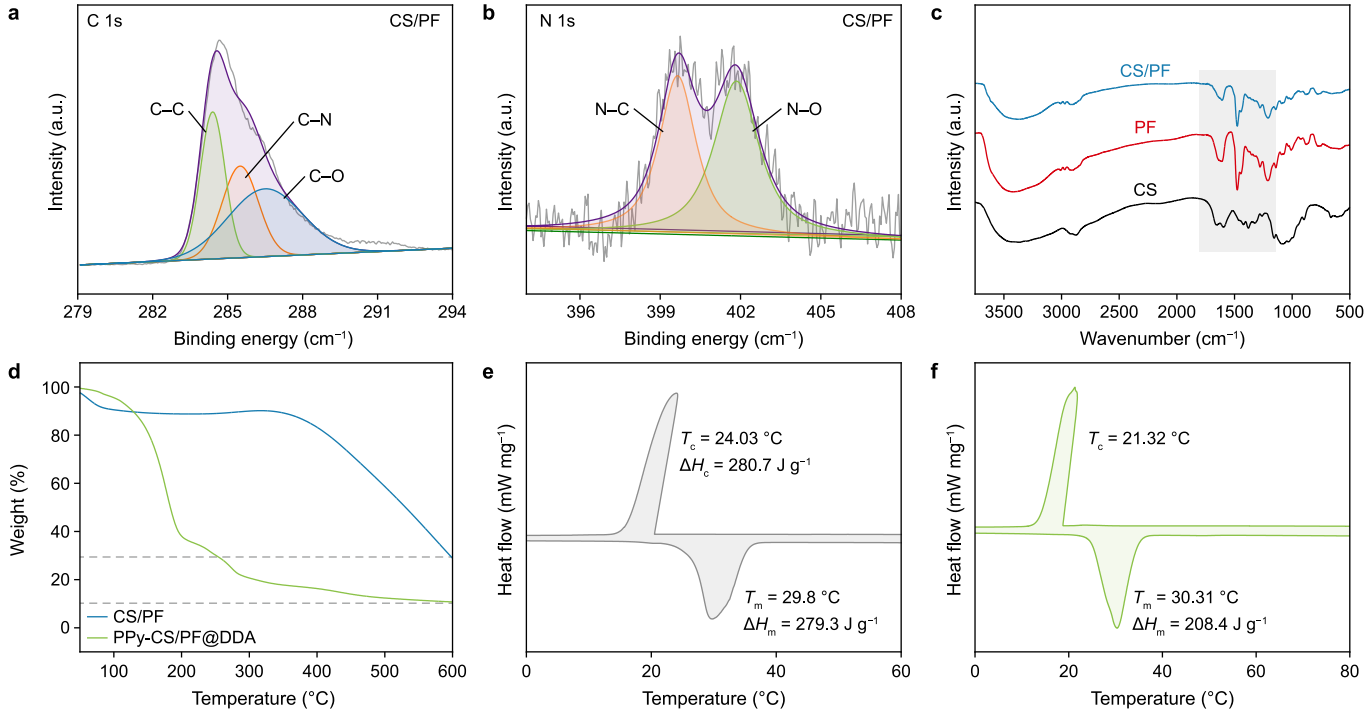

Fig. 2. Chemical composition and thermal properties of the PPy-CS/PF@DDA evaporator. a–b, X-ray photoelectron spectroscopy spectrum of CS/PF: C 1s (**a**) and N 1s (**b**). The grey curve represents the experimental spectrum, and the purple curve represents the fitted spectrum. **c**, Fourier transform infrared spectra of CS, PF, and CS/PF. The grey-shaded region highlights the main characteristic absorption region used for comparing functional group evolution. **d**, Thermogravimetric analysis curves of CS/PF and PPy-CS/PF@DDA. The horizontal dashed lines indicate the residual mass levels used for comparison. **e–f**, Differential scanning calorimetry curves of DDA (**e**) and PPy-CS/PF@DDA (**f**). PPy: polypyrrole; CS: chitosan; PF: phenolic resin; DDA: dodecylamine. T_c, T_m, and ΔH_m represent the crystallization temperature, melting temperature, and melting enthalpy, respectively.

melting temperatures show slight deviations compared to those of pure DDA, the thermal peaks remain prominent. This suggests that DDA retains good reversible phase change behavior within the composite structure. The minor differences in transition temperatures and enthalpy values are likely due to changes in the microenvironment of the DDA molecules induced by the incorporation of the PPy-CS/PF matrix. On the one hand, the interconnected three-dimensional porous structure of the PPy-CS/PF framework can effectively adsorb and immobilize DDA molecules, restricting their molecular mobility. On the other hand, this structure provides abundant nucleation sites, which facilitate the formation of more complete crystal structures and improve overall crystallization efficiency [51]. Moreover, DSC curves indicate that despite the structural constraints imposed by the supporting matrix, the composite still exhibits a relatively high phase-change enthalpy. Therefore, the PPy-CS/PF@DDA composite inherits DDA's excellent thermal energy storage capability and enables effective control over the phase-change process.

3.2. Properties and characteristics of PPy-CS/PF foam

The PPy-CS/PF foam exhibits exceptional hydrophilicity and water transport capabilities, which are essential for an efficient water supply during interfacial evaporation. Dynamic contact angle measurements show that a 1 μL water droplet is fully absorbed by the PPy-CS/PF surface within 15 ms (Fig. 3a). This phenomenon can be attributed to the material's intrinsic hydrophilicity and its highly porous internal structure. These pores significantly accelerate the transfer rate of water and salt ions, thereby providing an effective pathway for the rapid absorption and transport of water during solar interfacial evaporation. Consequently, the PPy-CS/PF material demonstrates highly efficient water supply capabilities during solar evaporation. In addition to hydrophilicity, the thermal insulation properties of photothermal evaporation materials are important for evaporation efficiency. To assess its heat-insulating effect, a 1 cm PPy-CS/PF sample was heated for 5 min using an alcohol lamp (Fig. 3b), with a fresh leaf placed on its surface. The leaf remained neither wilted nor discolored, indicating that the material possesses excellent thermal insulation. This property ensures that the heat from the heating source is effectively concentrated on the evaporation surface, minimizing heat loss and substantially increasing the water evaporation rate. By retaining heat at the evaporation surface, the PPy-CS/PF material maximizes solar energy utilization and promotes efficient water evaporation.

Furthermore, superior mechanical strength is essential for the long-term stability and durability of solar steam generation devices. The maximum compressive load that PPy-CS/PF material can withstand is 0.516 MPa, while its maximum tensile strength is 0.003 MPa (Fig. 3c). These properties endow the material with considerable compressive and tensile strength, allowing it to withstand repeated use (Supplementary Fig. S2 and Table S2). Consequently, the PPy-CS/PF material is well-suited for long-term use in complex environments, such as solar steam generation systems. In addition to its mechanical properties (Fig. 3d), the chemical stability of PPy-CS/PF material is also of paramount importance, particularly for applications in harsh environments. To evaluate the corrosion resistance of the PPy-CS/PF composite foam, it was immersed in a highly acidic solution (pH = 1) for 24 h. The material exhibited no appreciable swelling, structural collapse, or degradation under these harsh acidic conditions, demonstrating excellent chemical stability. Further evaluation under mechanical stress revealed that after 10 h of ultrasonic treatment, the foam retained its three-dimensional framework, with no evidence of fracture or interfacial delamination.

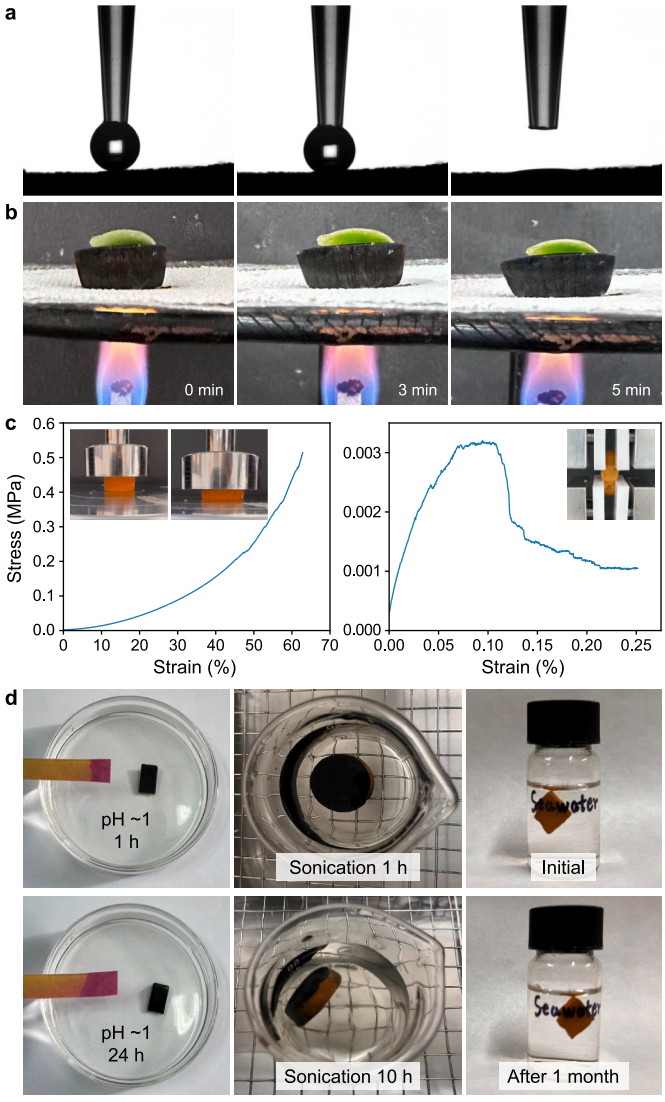

Fig. 3. Wettability, mechanical behavior, and stability of PPy-CS/PF. a, Representative sequential snapshots from a high-speed video, showing the dynamic wetting angle and rapid water-droplet absorption process on the surface of PPy-CS/PF. **b**, Digital photograph of a leaf placed on an alcohol lamp flame, illustrating the thermal insulation effect. **c**, Stress-strain curves of PPy-CS/PF. The inset images show the sample before and during the compression test (left), and during the tensile test (right). **d**, Digital photographs of PPy-CS/PF after treatment under acidic conditions (pH = 1, 24 h), ultrasonic agitation for 24 h, and immersion in seawater for 1 month, demonstrating its structural stability under harsh environments. PPy: polypyrrole; CS: chitosan; PF: phenolic resin; DDA: dodecylamine.

Furthermore, after one month of prolonged exposure to natural seawater, the foam retained its original morphology and structural framework without significant deterioration. These results collectively demonstrate that the PPy-CS/PF composite possesses exceptional chemical stability in extreme acidic environments as well as superior mechanical resilience and long-term durability.

3.3. Solar vapor generation of PPy-CS/PF@DDA solar evaporators

As independent evaporator materials, PPy-CS/PF and PPy-CS/PF@DDA feature a well-developed porous structure and demonstrate excellent light-harvesting capability and sustained photothermal conversion performance-both essential for long-term, stable operation. As shown in the ultraviolet-visible-NIR spectra

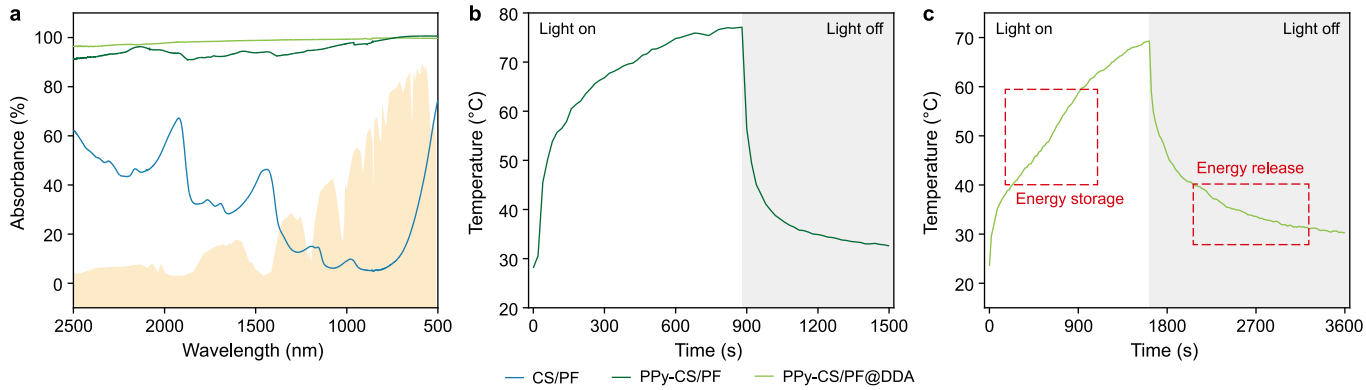

Fig. 4. Light absorption and photothermal conversion performance of the evaporators. **a**, Light absorption spectra of CS/PF, PPy-CS/PF, and PPy-CS/PF@DDA. The yellow-shaded area represents the solar spectrum over the corresponding wavelength range. **b**–**c**, Light to thermal conversion curves of PPy-CS/PF (**b**) and PPy-CS/PF@DDA (**c**). PPy: polypyrrole; CS: chitosan; PF: phenolic resin; DDA: dodecylamine.

(Fig. 4a), PPy-CS/PF and PPy-CS/PF@DDA exhibit high broadband solar absorption, reaching 92% and 95%, respectively, across the 500–2500 nm wavelength range. The incorporation of PPy markedly improves the optical absorption of the composite, raising it from 60% (in CS/PF) to 92%, thereby confirming the central role of PPy in improving the material's solar energy utilization efficiency. Regarding photothermal response, both PPy-CS/PF@DDA and PPy-CS/PF exhibit outstanding, rapid solar-to-thermal conversion performance. Specifically, at a light intensity of 1 kW m^{-2}, the surface temperature of PPy-CS/PF rapidly increases to 78 °C within 900 s and then remains stable, reflecting its excellent thermal stability (Fig. 4b). Upon turning off the light source, the temperature quickly returns to ambient conditions. In comparison, PPy-CS/PF@DDA exhibits a similarly rapid initial temperature increase (Fig. 4c), followed by the emergence of a thermal plateau corresponding to heat absorption and storage by the phase change material. Once the phase transition is complete, the temperature continues to rise. After the light source is turned off, the material undergoes an initial sharp temperature drop, followed by a slower decline that stabilizes at a secondary plateau, indicating the gradual release of latent heat. This dynamic thermal behavior illustrates the dual functionality of PPy-CS/PF@DDA in both efficient solar energy conversion and effective thermal energy storage.

To further assess the evaporative performance of the fabricated evaporators, we developed an experimental system that incorporated a simulated solar irradiance source, an infrared thermography system, an electronic analytical balance, and an evaporator sample (Supplementary Fig. S3). The surface temperature variations of the evaporators under simulated solar irradiation of 1 kW m^{-2} were monitored using infrared thermography. The surface temperature of the PPy-CS/PF evaporator increased from 41.2 °C at 5 min to 44.2 °C at 30 min (Fig. 5a and b), significantly exceeding that of the CS/PF evaporator, thus confirming that the incorporation of PPy substantially improves the material's light-to-heat conversion efficiency. Similarly, the surface temperature of the PPy-CS/PF@DDA evaporator increased from 36.3 to 43.0 °C under the same experimental conditions. This temperature rise followed a trend similar to that of the PPy-CS/PF evaporator, indicating that the capability.

Subsequently, the water evaporation rate of each evaporator was quantitatively measured using an electronic analytical balance (Fig. 5c) (The calculation formula can be found in Supplementary Text S2). The CS/PF evaporator exhibited an evaporation rate of 1.252 kg m^{-2} h^{-1}, approximately three times that of pure water (0.409 kg m^{-2} h^{-1}). The PPy-CS/PF evaporator demonstrated a marked improvement in evaporation rate, reaching 1.863 kg m^{-2} h^{-1}, indicating that PPy significantly increases the material's evaporative capacity. Meanwhile, the evaporation rate of the PPy-CS/PF@DDA evaporator was 1.862 kg m^{-2} h^{-1}, nearly identical to that of PPy-CS/PF, suggesting that the addition of DDA does not adversely affect evaporation performance (Supplementary Table S3). Moreover, when the light power density increased to 2 and 3 kW m^{-2}, the evaporation rate of the PPy-CS/PF@DDA evaporator further increased to 2.950 and 4.140 kg m^{-2} h^{-1}, respectively. These findings demonstrate the light-to-heat conversion efficiency and stable performance of the PPy-CS/PF@DDA evaporator under high light-intensity conditions, indicating its suitability for operation in environments with varying irradiance levels.

This study also assessed the photothermal conversion efficiency and thermal energy storage capacity of PPy-CS/PF and PPy-CS/PF@DDA foams through controlled simulations of solar radiation, with experimental results (Fig. 5d). During the illumination phase, the temperature of all materials increased rapidly, but PPy-CS/PF@DDA foam reached a distinct temperature plateau at approximately 37.0 °C, indicating the commencement of the energy storage process. Upon removal of the light source, the cooling rate of PPy-CS/PF@DDA was significantly slower than that of the other materials, maintaining a higher temperature for an extended period and demonstrating its superior ability to retain thermal energy. This suggests that PPy-CS/PF@DDA effectively stores thermal energy, thereby prolonging its thermal effect and improving its potential for continuous operation. In parallel, the water mass loss during the evaporation process was continuously monitored (Fig. 5e). After 30 min of solar exposure, the evaporation rates of both PPy-CS/PF and PPy-CS/PF@DDA were nearly identical. However, upon removal of the light source, the evaporation rate of PPy-CS/PF@DDA (0.684 kg m^{-2} h^{-1}) slightly exceeded that of PPy-CS/PF (0.626 kg m^{-2} h^{-1}). This difference illustrates the contribution of the DDA phase-change material, which improves the composite's ability to convert some of the absorbed thermal energy into latent heat storage. This extends the evaporator's effective operational time and improves its sustained evaporation performance.

In addition, to evaluate the stability of the PPy-CS/PF@DDA composite during repeated photothermal cycles (Supplementary Fig. S4), a series of 15 consecutive heating-cooling alternating tests was conducted (Fig. 5f). The average evaporation rate in the 1-sun conditions was 1.825 kg m^{-2} h^{-1} throughout each cycle, while the average evaporation rate in darkness was

0.647 kg m^{-2} h^{-1}. These results confirm that the PPy-CS/PF@DDA composite exhibits excellent long-term stability and reliability, effectively preserving its photothermal conversion and energy storage performance during prolonged operation.

3.4. Salt rejection ability

Salt rejection is an important performance parameter for evaluating whether an evaporator can operate stably during long-term seawater desalination. To systematically assess the evaporation performance of PPy-CS/PF@DDA foam under high-salinity conditions and its adaptability to varying salt concentrations, a series of evaporation experiments was conducted. Under simulated solar illumination at 1 kW m^{-2}, the evaporation rates of PPy-CS/PF@DDA in 3.5 wt%, 5 wt%, 10 wt%, 15 wt%, and 20 wt% NaCl solutions were 1.801, 1.790, 1.786, 1.772, and 1.763 kg m^{-2} h^{-1}, respectively (Fig. 6a). Although a slight decrease in evaporation rate was observed with increasing salt concentration, the overall rates remained high, with fluctuations within 2.1%. These results indicate that the material maintains efficient photothermal evaporation performance, even under high-salinity conditions.

To further investigate the material's response to different salt types, evaporation tests were conducted using three representative salt solutions at identical concentrations (5 wt% NaCl, $MgCl_2$, and $MgSO_4$). The corresponding evaporation rates were 1.801, 1.796, and 1.792 kg m^{-2} h^{-1}, respectively (Fig. 6b and c), with the mass-versus-time curves exhibiting nearly identical trends. These results suggest that the photothermal performance of the PPy-CS/PF@DDA foam remains consistently stable in the presence of various salt types. Furthermore, to evaluate long-term operational stability under high salinity, a continuous 2-h solar-driven evaporation test was performed in a 20 wt% NaCl solution (Fig. 6d). During the initial phase, the evaporation rate increased rapidly and subsequently reached a steady state. Post-experiment imaging revealed no observable salt crystallization on the evaporator surface, and the surface remained structurally intact. This resistance to salt accumulation is attributed to the foam's interconnected porous network, which promotes efficient backflow and diffusion of salt ions, thereby preventing salt precipitation at the evaporation interface. Such structural features play an important role in maintaining long-term evaporation efficiency and durability [52], even under highly saline conditions.

3.5. Wastewater treatment and outdoor measurements

We assessed the desalination and wastewater purification capabilities of PPy-CS/PF@DDA foam using natural seawater collected from Shilaoren Beach in Qingdao, China, and artificially prepared heavy metal solutions containing 20 mg L^{-1} of metal ions. Inductively coupled plasma mass spectrometry analysis (Fig. 7a) revealed that, following treatment, the concentrations of key seawater ions—Na^+, K^+, Ca^{2+}, and Mg^{2+}—were reduced by two to three orders of magnitude relative to their initial values, achieving levels compliant with WHO drinking water standards [24,53]. Simultaneously, in synthetic wastewater containing Ni^{2+}, Cu^{2+}, Zn^{2+}, and Cd^{2+}, the concentrations of these heavy metal ions decreased significantly to 0.010, 0.0136, 0.074, and 0.004 mg L^{-1}, respectively (Fig. 7b), all well below conventional regulatory discharge thresholds [54]. These results indicate that the material exhibits excellent efficiency in seawater purification and the removal of heavy metal pollutants.

To evaluate the removal of organic pollutants, a photothermal evaporation experiment was conducted using methyl orange as a representative model compound. The condensed water collected

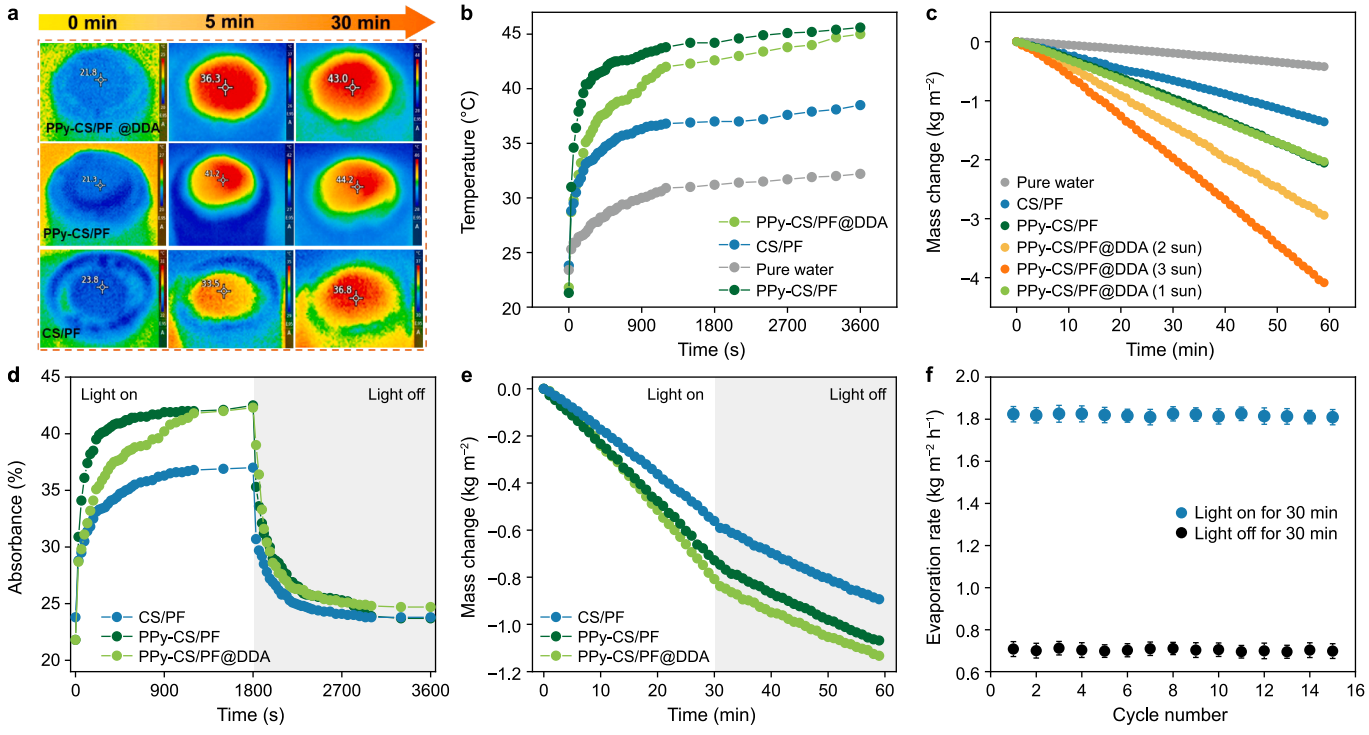

Fig. 5. Photothermal response, evaporation behavior, and cycling stability of PPy-CS/PF@DDA. a, Surface temperature variation of the evaporator. **b**, Surface temperature versus time of evaporator with illumination of 1 kW m^{-2} **c**, Mass change of water over time under different illuminations (1 sun, 2 sun, and 3 sun illumination). **d**, Surface temperature versus time under 1 kW m^{-2} light and after the removal of light. **e**, Mass change of water over time under 1 kW m^{-2} light and after the removal of light. **f**, Evaporation rate of PPy-CS/PF@DDA with illumination of 1 kW m^{-2} for 15 cycles. PPy: polypyrrole; CS: chitosan; PF: phenolic resin; DDA: dodecylamine.

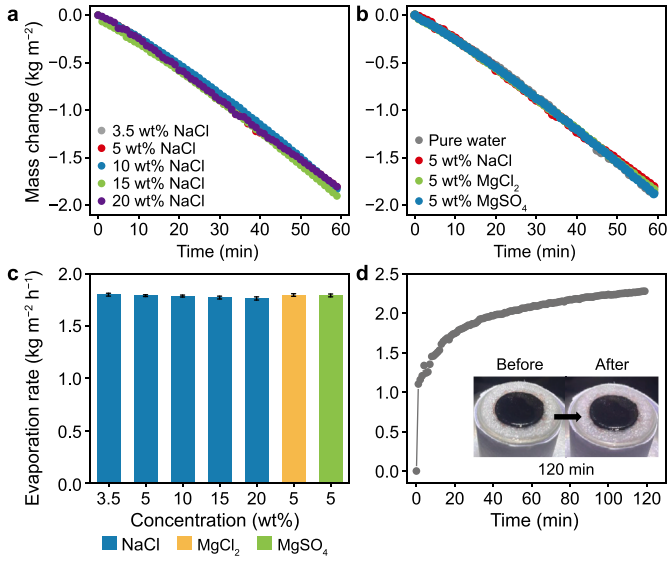

Fig. 6. Salt rejection and long-term evaporation performance of PPy-CS/PF@DDA in saline water. a, Mass change of water over time with different NaCl concentrations under illumination (1 kW m^{-2}). **b**, Mass change of different salt types under illumination (1 kW m^{-2}). **c**, Steam evaporation rate with different NaCl concentrations and different salt types under illumination (1 kW m^{-2}). **d**, Evaporation rate of PPy-CS/PF@DDA in NaCl (5 wt%) under 1 sun illumination at different times. Inset images are the surface pictures of PPy-CS/PF@DDA before and after immersion in NaCl (20 wt%) for 120 min. PPy: polypyrrole; CS: chitosan; PF: phenolic resin; DDA: dodecylamine.

after evaporation appeared colorless and transparent, and its ultraviolet and visible spectrophotometer absorption spectrum (Fig. 7c) showed no detectable absorption peak at 465 nm. This confirms that under solar irradiation, PPy-CS/PF@DDA selectively evaporates water while retaining nonvolatile organic species from the source solution, enabling efficient separation and recovery of clean water.

Building on the above results, we assessed the long-term performance of the evaporator under realistic outdoor conditions through a field test. On July 2, 2024, from 8:00 to 17:00, we deployed a solar evaporation system on the outdoor platform of Ocean University of China (Fig. 7d), with natural sunlight as the sole energy source (humidity fluctuated between 65% and 75% under light-breeze conditions). The system comprised a hemispherical acrylic collector for condensate and a bottom layer consisting of ten PPy-CS/PF@DDA foam modules (2.1 cm × 2.1 cm × 0.75 cm each) arranged to form the evaporation interface. The evaporation rate exhibited a clear correlation with fluctuations in solar irradiance and ambient temperature (Fig. 7e and f). A peak evaporation rate of 1.583 kg m^{-2} h^{-1} was recorded between 11:00 and 13:00, corresponding to the period of highest solar intensity. After 10 h of continuous operation, the total freshwater output reached 9.229 kg m^{-2}, approximately 4.7 times that of seawater PPy-CS/PF@DDA evaporated under the same conditions, demonstrating both the high efficiency and operational stability of the PPy-CS/PF@DDA-based evaporator under natural sunlight. Moreover, the material cost of PPy-CS/PF@DDA remains low ($0.54 m^{-2}), and the fabrication process is

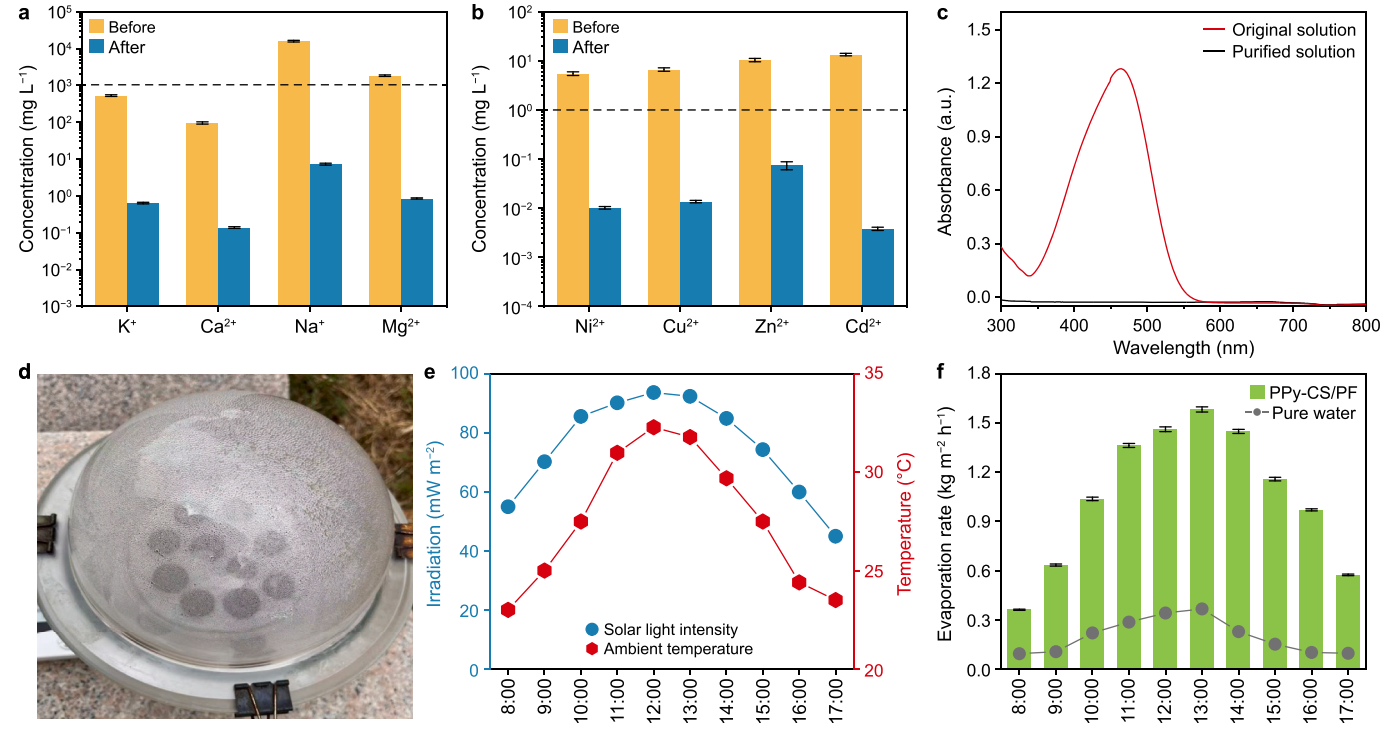

Fig. 7. Desalination, wastewater purification, and outdoor evaporation performance of PPy-CS/PF@DDA. a, Concentrations of the major ions in seawater from Shilaoren Beach before and after desalination. **b**, Concentrations of four heavy metal ions in wastewater before and after solar-driven purification. The dashed line indicates the World Health Organization standard. **c**, Ultraviolet-visible-NIR absorption spectra of methyl orange solution before and after purification. The inset shows digital photographs of the dye solution before and after purification. **d**, Digital photographs of PPy-CS/PF@DDA. **e**, Solar light intensity and ambient temperature recorded during the outdoor test. **f**, Evaporation rates of PPy-CS/PF@DDA in seawater and those of natural seawater evaporation under outdoor conditions. PPy: polypyrrole; CS: chitosan; PF: phenolic resin; DDA: dodecylamine.

straightforward (Supplementary Table S4–S5). These advantages suggest a strong potential for large-scale deployment in solar desalination systems.

4. Conclusion

In summary, we developed a PPy-CS/PF@DDA composite foam evaporator that integrates high photothermal conversion efficiency with phase change energy storage capability. Through the synergistic effect of its three-dimensional porous framework and embedded phase change units, the material achieves 95% broadband solar absorption and a latent heat storage capacity of 208.4 J g^{-1}. Under 1-sun irradiation (1 kW m^{-2}), it delivers an evaporation rate of 1.862 kg m^{-2} h^{-1}, representing a 48.7% improvement over unmodified foams while maintaining stable performance during prolonged light–dark cycling. Notably, the evaporator demonstrates robust operation in hypersaline environments (0–20 wt% NaCl), preventing salt crystallization and sustaining continuous freshwater production of 9.229 kg m^{-2} over 10 h, pointing to its excellent salt resistance and practical applicability. This study introduces an effective strategy to mitigate evaporation fluctuations caused by intermittent solar irradiation and establishes a sustainable approach for mitigation, further concentration, and purification of high-salinity brine, thereby facilitating the practical implementation of solar-driven interfacial evaporation in seawater desalination and the treatment of complex wastewater.

CRediT authorship contribution statement

Peilei Zhou: Writing – review & editing, Writing – original draft, Visualization, Validation, Methodology, Formal analysis, Data curation, Conceptualization. **Feng Sun:** Supervision. **Lishan Xu:** Validation. **Qingshan Liu:** Resources. **Jia Xu:** Supervision, Resources, Funding acquisition.

Declaration of competing interest

The authors declare that they have no known competing financial interests or personal relationships that could have appeared to influence the work reported in this paper.

Acknowledgements

This work was supported by the National Natural Science Foundation of China (No. 22378374) and the National Natural Science Foundation of Shandong Province (No. ZR2024MB086).

Appendix A. Supplementary data

Supplementary data to this article can be found online at https://doi.org/10.1016/j.ese.2026.100696.

Data availability

Data will be made available on request.

References

[1] J. Hu, Y. Sun, Z. Liu, B. Zhu, L. Zhang, N. Xu, M. Zhu, J. Zhu, Z. Chen, Photothermal fabrics for solar-driven seawater desalination, Prog. Mater. Sci. 150 (2025) 101407.
[2] M. Elimelech, W.A. Phillip, The future of seawater desalination: energy, technology, and the environment, Science 333 (6043) (2011) 712–717.
[3] S. Lin, H. Zhao, L. Zhu, T. He, S. Chen, C. Gao, L. Zhang, Seawater desalination technology and engineering in China: a review, Desalination 498 (2021) 114728.
[4] L. Wang, X. Sun, F. Gao, Y. Yang, R. Song, Solar membrane distillation: an emerging technology for reverse osmosis concentrated brine treatment, Desalination 592 (2024) 118124.
[5] B.K. Pramanik, L. Shu, V. Jegatheesan, A review of the management and treatment of brine solutions, Environ. Sci.: Water Res. Technol. 3 (4) (2017) 625–658.
[6] L. Cui, C. Ma, P. Wang, H. Che, H. Xu, Y. Ao, Rationally constructing a 3D bifunctional solar evaporator for high-performance water evaporation coupled with pollutants degradation, Appl. Catal. B Environ. 337 (2023) 122988.
[7] L. Zayani, R. Rokbani, M. Trablesi-Ayedi, Study of the evaporation of a brine involving the system Na+, Mg 2+, K+, cl−, S, J. Therm. Anal. Calorim. 57 (2) (1999) 575–585.
[8] R. Katal, T.Y. Shen, I. Jafari, S. Masudy-Panah, M.H.D.A. Farahani, An overview on the treatment and management of the desalination brine solution. Desalination-Challenges and Opportunities, 2020.
[9] N. Ahmad, R.E. Baddour, A review of sources, effects, disposal methods, and regulations of brine into marine environments, Ocean Coast Manag. 87 (2014) 1–7.
[10] L. Cui, P. Wang, H. Che, X. Gao, J. Chen, B. Liu, Y. Ao, Environmental energy enhanced solar-driven evaporator with spontaneous internal convection for highly efficient water purification, Water Res. 244 (2023) 120514.
[11] N.C. Darre, G.S. Toor, Desalination of water: a review, Curr. Pollut. Rep. 4 (2) (2018) 104–111.
[12] A. Panagopoulos, K.-J. Haralambous, M. Loizidou, Desalination brine disposal methods and treatment technologies-A review, Sci. Total Environ. 693 (2019) 133545.
[13] H. Jin, J. Xu, H. Liu, H. Shen, H. Yu, M. Jaroniec, Y. Zheng, S.-Z. Qiao, Emerging materials and technologies for electrocatalytic seawater splitting, Sci. Adv. 9 (42) (2023) eadi7755.
[14] A. Panagopoulos, Brine management (saline water & wastewater effluents): sustainable utilization and resource recovery strategy through Minimal and Zero Liquid Discharge (MLD & ZLD) desalination systems, Chem. Eng. Process. Process Intensif. 176 (2022) 108944.
[15] K.M. Shah, I.H. Billinge, X. Chen, H. Fan, Y. Huang, R.K. Winton, N.Y. Yip, Drivers, challenges, and emerging technologies for desalination of high-salinity brines: a critical review, Desalination 538 (2022) 115827.
[16] A. Panagopoulos, V. Giannika, Techno-economic analysis (TEA) of zero liquid discharge (ZLD) systems for treatment and utilization of brine via resource recovery, Chem. Eng. Process. Process Intensif. 200 (2024) 109773.
[17] Y. Zheng, Z. Zhu, S. Liang, X. Ma, Concentrated solar supercritical water desalination and multi-effect distillation hybrid systems for efficient zero liquid discharge, Desalination 609 (2025) 118890.
[18] P. Calleja-Cayón, P. Hernández-Baño, A. Molina-García, F. Vera-García, Mechanical vapour compression modelling and assessment in a zero-liquid-discharge desalination system, Processes 13 (7) (2025) 1963.
[19] T.V. Bartholomew, L. Mey, J.T. Arena, N.S. Siefert, M.S. Mauter, Osmotically assisted reverse osmosis for high salinity brine treatment, Desalination 421 (2017) 3–11.
[20] J.A. Bush, J. Vanneste, T.Y. Cath, Membrane distillation for concentration of hypersaline brines from the Great Salt Lake: effects of scaling and fouling on performance, efficiency, and salt rejection, Separ. Purif. Technol. 170 (2016) 78–91.
[21] D.W. Johnson, N. Muppavarapu, H.J. Shipley, Aeration waste heat for membrane evaporation of desalination brine concentrate, J. Membr. Sci. 539 (2017) 1–13.
[22] A. Panagopoulos, V. Giannika, A comprehensive assessment of the economic and technical viability of a zero liquid discharge (ZLD) hybrid desalination system for water and salt recovery, J. Environ. Manag. 359 (2024) 121057.
[23] T. Tong, L. Xu, T. Horseman, P. Westerhoff, P. Xu, Y. Yao, X. Zhang, R. Alghanayem, S. Lin, Brine management with zero and minimal liquid discharge, Nat. Rev. Clean Technol. (2025) 1–16.
[24] H.T. Kim, L. Philip, A. McDonagh, M. Johir, J. Ren, H.K. Shon, L.D. Tijing, Recent advances in high-rate solar-driven interfacial evaporation, Adv. Sci. 11 (26) (2024) 2401322.
[25] S. kumar Balu, S. Cheng, S.S. Latthe, R. Xing, S. Liu, Solar-driven interfacial evaporation: materials design and device assembly, Energy Mater. 4 (2) (2024). N/A-N/A.
[26] M. Zhou, L. Zhang, S. Tao, R. Li, Y. Wang, Recent research advances in efficient solar-driven interfacial evaporation, Chem. Eng. J. 489 (2024) 151157.
[27] L. Cui, P. Wang, H. Che, X. Gao, J. Chen, B. Liu, Y. Ao, Co nanoparticles modified N-doped carbon nanosheets array as a novel bifunctional photothermal membrane for simultaneous solar-driven interfacial water evaporation and persulfate mediating water purification, Appl. Catal. B Environ. 330 (2023) 122556.
[28] Y. Fang, H. Gao, K. Cheng, L. Bai, Z. Li, Y. Zhao, X. Xu, An overview of photothermal materials for solar-driven interfacial evaporation, Chin. Chem. Lett. 36 (3) (2025) 109925.
[29] Y. Sun, X. Tan, X. Yuan, J. Li, Solar-driven interfacial evaporation: research advances in structural design, Chem. Eng. J. 495 (2024) 153316.
[30] S. Guo, Y. Zhang, H. Qu, M. Li, S. Zhang, J. Yang, X. Zhang, S.C. Tan, Repurposing face mask waste to construct floating photothermal evaporator for autonomous solar ocean farming, EcoMat 4 (2) (2022) e12179.
[31] J. Liu, S. Zhang, J. Wang, Q. Lan, Recent progress in solar-driven interfacial

evaporation: evaporators, condensers, applications and prospects, Desalination 597 (2025) 118356.
[32] J. Li, L. Mu, Q. Liu, Y. Zhang, R. Zhang, X. Zhu, C.-L. Sun, J. He, M. Qu, A review: fabric-based solar driven interfacial evaporator, Nano Energy 132 (2024) 110394.
[33] S. Guo, Y. Zhang, S.C. Tan, Device design and optimization of sorption-based atmospheric water harvesters, Device 1 (4) (2023).
[34] Y. Xiao, H. Guo, M. Li, J. He, X. Xu, S. Liu, L. Wang, T.D. James, Strategies for enhancing the photothermal conversion efficiency of solar-driven interfacial evaporation, Coord. Chem. Rev. 527 (2025) 216378.
[35] S. Guo, S. Patel, J. Wang, Z. Yu, H. Qu, S. Zhang, K. Yu, S. Liu, J.J. Koh, X.Q. Koh, Self-powered green energy–harvesting and sensing interfaces based on hygroscopic gel and water-locking effects, Sci. Adv. 11 (27) (2025) eadw5991.
[36] S. Guo, Y. Zhang, Z. Yu, M. Dai, X. Liu, H. Wang, S. Liu, J.J. Koh, W. Sun, Y. Feng, Leaf-based energy harvesting and storage utilizing hygroscopic iron hydrogel for continuous power generation, Nat. Commun. 16 (1) (2025) 5267.
[37] L. Hou, S. Li, Y. Qi, J. Liu, Z. Cui, X. Liu, Y. Zhang, N. Wang, Y. Zhao, Advancing efficiency in solar-driven interfacial evaporation: strategies and applications, ACS Nano 19 (10) (2025) 9636–9683.
[38] Q. Chen, H. Zhang, L. Zou, R. Yang, G. Zeng, P. Lin, L. Yang, M. Zheng, X. Li, Solar interfacial evaporation hydrogel with distributed packaging of phase change materials for continuous desalination, Chem. Eng. J. 506 (2025) 160061.
[39] P. Liu, X. Chen, Y. Li, P. Cheng, Z. Tang, J. Lv, W. Aftab, G. Wang, Aerogels meet phase change materials: fundamentals, advances, and beyond, ACS Nano 16 (10) (2022) 15586–15626.
[40] V. Goel, A. Saxena, M. Kumar, A. Thakur, A. Sharma, V. Bianco, Potential of phase change materials and their effective use in solar thermal applications: a critical review, Appl. Therm. Eng. 219 (2023) 119417.
[41] H. Sun, P. Zhou, W. Zhang, J. Li, Z. Zhu, C. Ma, W. Liang, A. Li, Flexible and double-layered photothermal material based on resorcinol-formaldehyde foam for solar assisted water desalination, Sol. Energy Mater. Sol. Cell. 232 (2021) 111350.
[42] F. Liu, W. Liang, C. Wang, C. Xiao, J. He, G. Zhao, Z. Zhu, H. Sun, A. Li, Superhydrophilic and mechanically robust phenolic resin as double layered photothermal materials for efficient solar steam generation, Mater. Today Energy 16 (2020) 100375.
[43] L. Wang, W. Liang, C. Wang, Y. Fan, Y. Liu, C. Xiao, H. Sun, Z. Zhu, A. Li, Dodecylamine/Ti3C2-pectin form-stable phase change composites with enhanced light-to-thermal conversion and mechanical properties, Renew. Energy 176 (2021) 663–674.
[44] Z.-L. Yu, Z.-Y. Wu, S. Xin, C. Qiao, Z.-Y. Yu, H.-P. Cong, S.-H. Yu, General and straightforward synthetic route to phenolic resin gels templated by chitosan networks, Chem. Mater. 26 (24) (2014) 6915–6918.
[45] S. Zhang, J. Feng, J. Feng, Y. Jiang, Oxidation-mediated chitosan as additives for creation of chitosan aerogels with diverse three-dimensional interconnected skeletons, Appl. Surf. Sci. 396 (2017) 1220–1225.
[46] B. Gullón, M.I. Montenegro, A.I. Ruiz-Matute, A. Cardelle-Cobas, N. Corzo, M.E. Pintado, Synthesis, optimization and structural characterization of a chitosan–glucose derivative obtained by the Maillard reaction, Carbohydr. Polym. 137 (2016) 382–389.
[47] T.E. Douglas, S. Kumari, K. Dziadek, M. Dziadek, A. Abalymov, P. Cools, G. Brackman, T. Coenye, R. Morent, M. Mohan, Titanium surface functionalization with coatings of chitosan and polyphenol-rich plant extracts, Mater. Lett. 196 (2017) 213–216.
[48] S. Liu, B. Huang, L. Chai, Y. Liu, G. Zeng, X. Wang, W. Zeng, M. Shang, J. Deng, Z. Zhou, Enhancement of s (V) adsorption from aqueous solution by a magnetic chitosan/biochar composite, RSC Adv. 7 (18) (2017) 10891–10900.
[49] W. Wang, S. Liu, Y. Liu, W. Jing, R. Zhao, Z. Lei, Phenolic resin/chitosan composite derived nitrogen-doped carbon as highly durable and anti-poisoning electrocatalyst for oxygen reduction reaction, Int. J. Hydrogen Energy 42 (43) (2017) 26704–26712.
[50] X. Ye, Z. Tian, X. Cao, Y. Fan, P. Zhou, C. Wang, J. Li, H. Sun, Z. Zhu, W. Liang, Fatty amines embedded carbon membranes with aligned nanochannels network: a device with extremely high photothermal conversion efficiency toward solar energy harvesting and storage, Sol. RRL 6 (4) (2022) 2100924.
[51] X. Huang, X. Chen, A. Li, D. Atinafu, H. Gao, W. Dong, G. Wang, Shape-stabilized phase change materials based on porous supports for thermal energy storage applications, Chem. Eng. J. 356 (2019) 641–661.
[52] H. Yang, Y. Sun, M. Peng, M. Cai, B. Zhao, D. Li, Z. Liang, L. Jiang, Tailoring the salt transport flux of solar evaporators for a highly effective salt-resistant desalination with high productivity, ACS Nano 16 (2) (2022) 2511–2520.
[53] F. He, X. Wu, J. Gao, Z. Wang, Solar-driven interfacial evaporation toward clean water production: burgeoning materials, concepts and technologies, J. Mater. Chem. A 9 (48) (2021) 27121–27139.
[54] X. Xu, Q. Zhao, Q. Liu, et al., Full-spectrum-responsive Ti_4O_7-PVA nanocomposite hydrogel with ultrahigh evaporation rate for efficient solar steam generation, Desalination 577 (2024) 117400.